ADVANCED ENERGY MATERIALS
www.advenergymat.de

^{13}C-Labeled Mesoporous N-Doped Carbon Nanospheres and N-Doped Hydrothermal Carbon Aerogels as Model Materials for Carbon Corrosion Determination in Electrode Structures

*Niklas Ortlieb, Julian Martin, Lars Guggolz, Jari Ihonen, and Anna Fischer**

Carbon nanostructures are widely used in electrodes for energy storage and conversion applications due to their unique properties. Unfortunately, carbon materials can degrade under harsh oxidative electrochemical conditions, leading to carbon corrosion to CO and CO_2. Therefore, it is necessary to develop methods for in situ monitoring of carbon corrosion during system operation. In this work, ^{13}C labeling is introduced into mesoporous N-doped carbon nanospheres and N-doped hydrothermal carbon aerogels, allowing the selective detection of $^{13}CO_2$ via electrochemically coupled mass spectrometry during carbon corrosion. Different labeling degrees (unlabeled, partially and fully labeled) are achieved while maintaining the carbon material's morphology and physicochemical properties. These materials and mixtures of unlabeled and fully labeled materials are subjected to accelerated stress tests to evaluate their carbon corrosion behaviour. The results demonstrated that $^{13}CO_2$ can only be found in labeled samples, regardless of whether they are partially labeled or a mixture of unlabeled and fully labeled materials. This technique facilitates in situ detection of carbon corrosion, even in the presence of a CO_2 background in air. More importantly, it allows us to distinguish between corrosion originating from the carbon material itself and other carbon-containing components within electrochemical systems, thereby advancing the understanding of carbon materials in such systems.

1. Introduction

Carbon materials are widely used in electrode structures for energy storage and conversion applications due to their unique properties and versatility.[1] They exhibit excellent electric conductivity, light weight, chemical robustness, and nanostructure versatility, making them the ideal material for use in electrode structures, protective coatings, and structural support. Their high conductivity allows for efficient electron transfer, which is crucial for energy storage and conversion devices.[2] Additionally, carbon can form various allotropes and structures with different properties, including graphite, carbon nanotubes, graphene, activated carbon, and carbon nanofibers, which allows for tailoring carbon materials to specific energy applications.[3]

Many carbon materials, especially activated carbons, have extremely high surface areas (from several hundred up to several thousand $m^2\ g^{-1}$).[4] This property is essential for increasing the contact area between electrode material and electrolyte, enhancing charge storage capacity in supercapacitors and batteries, or providing more reaction sites for electrocatalysis in fuel cells and electrolysers. Additionally, the porous nature of many carbon materials facilitates ion transport and storage, which is crucial for the mentioned applications. The ability to control pore size and distribution hereby allows for optimizing ion accessibility and charge

N. Ortlieb, J. Martin, L. Guggolz, A. Fischer
Institute of Inorganic and Analytic Chemistry (IAAC), Inorganic Functional Materials and Nanomaterials
University of Freiburg
Albertstr. 21, 79104 Freiburg, Germany
E-mail: anna.fischer@ac.uni-freiburg.de

The ORCID identification number(s) for the author(s) of this article can be found under https://doi.org/10.1002/aenm.202406164

DOI: 10.1002/aenm.202406164

N. Ortlieb, J. Martin, L. Guggolz, A. Fischer
Freiburg Materials Research Center (FMF)
University of Freiburg
Stefan-Meier-Str. 21, 79104 Freiburg, Germany

A. Fischer
Freiburg Center of Interactive Materials and Bioinspired Technologies (FIT)
University of Freiburg
Georges-Köhler-Allee 105, 79110 Freiburg, Germany

N. Ortlieb, A. Fischer
Cluster of Excellence livMatS
University of Freiburg
Georges-Köhler-Allee 105, 79110 Freiburg, Germany

J. Ihonen
VTT Technical Research Centre of Finland Ltd.
P.O. Box 1000, FI-02044 VTT Espoo, Finland

storage.[5] Carbon materials can be easily functionalized or doped with other elements (e.g., nitrogen, boron, sulfur) to enhance their physicochemical and electrochemical properties.[6,7] This allows for fine-tuning of the material's performance (e.g., activity and/or stability) for specific applications. Many carbon materials, especially those derived from biomass, are relatively inexpensive and abundant, making them cost-effective for large-scale energy applications.[8]

In general, carbon materials are chemically stable, which contributes to the longevity and stability of electrochemical energy devices. Unfortunately, under harsh oxidative electrochemical environments, carbon corrosion/degradation to CO_2 (and CO) occurs, which is typically caused by electrochemical oxidation:

$$C + 2\,H_2O \rightarrow CO_2 + 4\,H^+ + 4e^- \qquad E^\circ = 0.207\ \text{V vs. SHE} \qquad (1)$$

$$C + H_2O \rightarrow CO + 2H^+ + 2e^- \qquad E^\circ = 0.518\ \text{V vs. SHE} \qquad (2)$$

This reaction occurs at elevated oxidative potentials, leading to the degradation of carbon-based electrode materials, and especially high anodic potentials above 0.8 V vs. SHE (standard hydrogen electrode) accelerate carbon corrosion.[9] Elevated temperatures and the presence of water can also exacerbate corrosion rates.[10]

In proton exchange membrane fuel cells (PEMFCs), carbon corrosion due to load changes may limit the PEMFC lifetime and degrade, amongst others, the catalyst's carbon support, therefore requiring the use of more stable supports, which can decrease the available electrochemically active surface area. Measuring carbon support corrosion due to load changes requires accelerated stress testing (AST) methods, which have, however, large uncertainties compared to real-life operation.[11] Carbon support corrosion also occurs in reactant starvation situations, which may lead to rapid loss of PEMFC lifetime due to loss of electrochemically active surface area, as well as electrode shrinkage.[12]

State-of-the-art techniques to study carbon corrosion at end-of-life are mainly based on post-mortem analysis, e.g., scanning electron microscopy (SEM), which is used to measure the remaining thickness of the catalyst layer. The drawbacks of these techniques are the destructive nature of the methods and that, in many cases, no information is obtained on where exactly and how degradation takes place. Therefore, it is necessary to develop materials and methods where the degradation can be followed in situ and in operando.

Differential Electrochemical Mass Spectrometry (DEMS),[13] Electrochemical Coupled Mass Spectrometry (EC-MS), or different laser spectrometer techniques (Tuneable Infrared Laser Absorption Spectroscopy–TILDAS, Cavity Ring-Down Spectroscopy–CRDS) allow for real-time detection of CO_2 generated from carbon corrosion (Equation (1)). To distinguish detected CO_2 from the $^{12}CO_2$ background of air and differentiate between carbon corrosion of different carbon components in the system, the use of ^{13}C isotope labeling could be applied to e.g. the carbon support, which then would allow the detection of $^{13}CO_2$ (1.1% of total CO_2 is normally $^{13}CO_2$ of natural abundance[14]) solely originating from the ^{13}C-labeled carbon support corrosion.

For example, the measurement of $^{13}CO_2$ could eliminate the need for $^{12}CO_2$ removal in PEMFC carbon corrosion measurements conducted under air at the cathode, and would allow for further improvement of the accuracy of carbon corrosion measurements.[11] If CO_2 removal is applied, when a ^{13}C-labeled carbon support is used, the expected improvement in accuracy is more than an order of magnitude based on the latest CRDS-based $^{13}CO_2$ measurement equipment available. This may enable measurement of catalyst carbon support corrosion in normal operation conditions. In measurements, where anode reactant starvation is detected by catalyst carbon support corrosion, the reactant starvation could be detected much earlier from $^{13}CO_2$ emission. However, both these measurements require that the ^{13}C-labeled carbon support has similar physicochemical properties and similar corrosion properties to the non-labeled carbon support used in the catalyst.

^{13}C isotope labeling has earlier been applied in material stability studies of lithium-ion batteries and carbon coatings.[15,16] However, ^{13}C isotope labeling is limited by the availability of suitable carbon materials with different degrees of labeling. Only if the used electrode material, which is already used for a certain electrochemical application, can be modified by ^{13}C labeling without changing its morphology and physicochemical properties, a diagnostic twin can be created and diagnostic functionality implemented into the electrode material and thus the electrochemical application.

Previously, we reported two different tailored mesoporous carbon systems, mesoporous Nitrogen-doped carbon nanospheres (MPNC) and Nitrogen-doped hydrothermal carbon aerogels (N-HTC) which can be used as high-performance electrode materials for the above-mentioned applications, such as supercapacitors,[5] batteries,[6] fuel cells[17,18] or water electrolysis (hydrogen evolution reaction).[19] Here we report an approach, where we were able to equip these materials with a diagnostic functionality, by introducing partial and full ^{13}C-labeling while preserving the morphology and other physicochemical properties of these materials, thereby generating ^{13}C-labeled diagnostic twins of the non-labeled materials. We then successfully used these materials to track carbon corrosion in unlabeled or fully labeled materials, in physical mixtures of unlabeled and fully labeled materials, as well as in partially labeled materials via EC-MS, demonstrating the diagnostic approach of the novel labeled carbon materials. With these materials in hand, researchers can now effectively distinguish the carbon corrosion of the e.g. catalyst support from other carbon materials implemented in electrochemical energy systems (e.g., the membrane, ionomer, binder, gas diffusion layer or bipolar plates of PEMFCs or carbon based coatings of metal bipolar plates, or the additive, binder, separator or current collector coatings in case of supercapacitors and aqueous batteries), thereby allowing to determine structure-stability correlations and to gain a better understanding of degradation processes and improve system durability and performance.

2. Results and Discussion

2.1. Unlabeled, Partially ^{13}C Labeled and Fully ^{13}C Labeled MPNC

To investigate the physicochemical properties of 50% and 100% ^{13}C-labeled MPNC nanospheres and to ensure that they do not differ from those of unlabeled nanospheres (with unlabeled meaning that the nanospheres contained the natural amount of

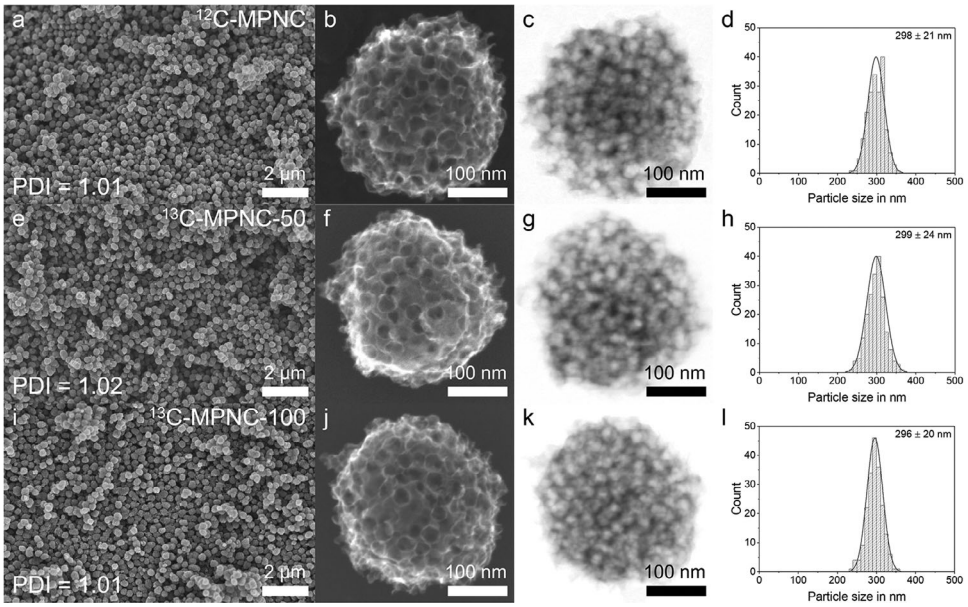

Figure 1. SEM and STEM images as well as particle size distribution of unlabeled (a–d), partially ^{13}C-labeled (e–h), and fully ^{13}C-labeled MPNC nanospheres. A polydispersity PDI < 1.10 is defined as monodisperse according to the IUPAC definition.[20]

1.1% ^{13}C), we first acquired SEM and STEM images (**Figure 1**). Unlabeled MPNC nanospheres showed uniform spherical particles with an average particle size of 298 nm and a polydispersity index PDI = 1.01 as defined by the IUPAC (Figure 1a–d). An index of 1.00 describes perfect monodispersity, but every value below 1.10 is still defined as monodisperse according to the IUPAC.[20] Our value of 1.01 indicates a narrow particle size distribution of the nanospheres and thereby nearly ideal monodispersity. In Figure 1c, the intraparticle porosity of the unlabeled nanospheres becomes evident from the STEM image. 50% ^{13}C labeled MPNC nanospheres (Figure 1e–h) revealed comparable resulting in an average particle size of 299 nm and a polydispersity index of PDI = 1.02. Again, the intraparticle porosity can be easily seen on the STEM image in Figure 1g. Finally, 100% ^{13}C-labeled MPNC nanospheres (Figure 1i–l) had an average particle size of 296 nm and a polydispersity index of PDI = 1.01, showing that there is no change in average particle size or particle size distribution with increasing level of ^{13}C labeling.

We then investigated the microstructure of the three samples by X-ray diffraction (XRD) and Raman spectroscopy, as well as the elemental composition by elemental combustion analysis (**Figure 2**). In the diffractogram of all samples (Figure 2a), the distinct broad (002) and (100) reflections of unordered carbon materials are visible at $2\theta = 23.5°$ and 43.7° ($\lambda = 1.54$ Å, Cu K_α).[21] Hereby,

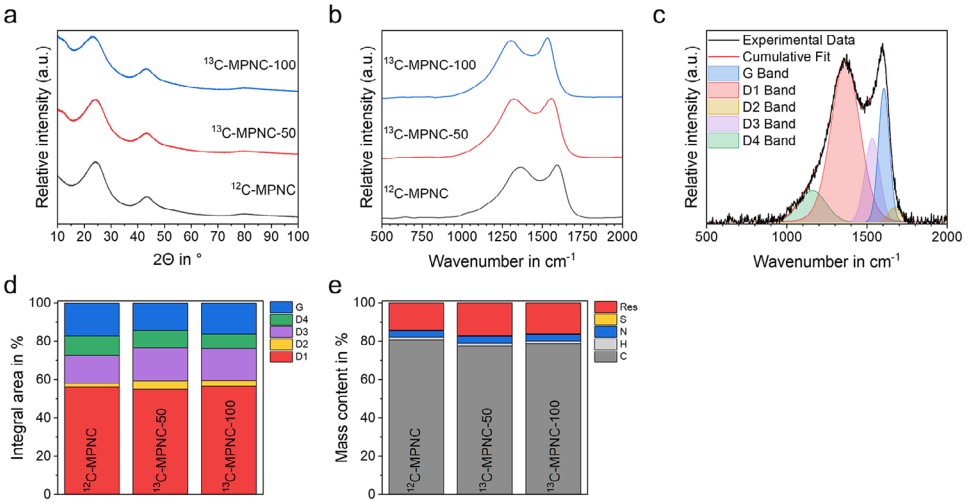

Figure 2. XRD diffractogram (a) and Raman spectrum (b) of unlabeled, partially ^{13}C-labeled, and fully ^{13}C-labeled MPNC nanospheres. Exemplary Raman deconvolution (c) for unlabeled MPNC (for all deconvolutions see Figure S1, Supporting Information) as well as integral areas (d). Elemental composition determined by elemental combustion analysis (e).

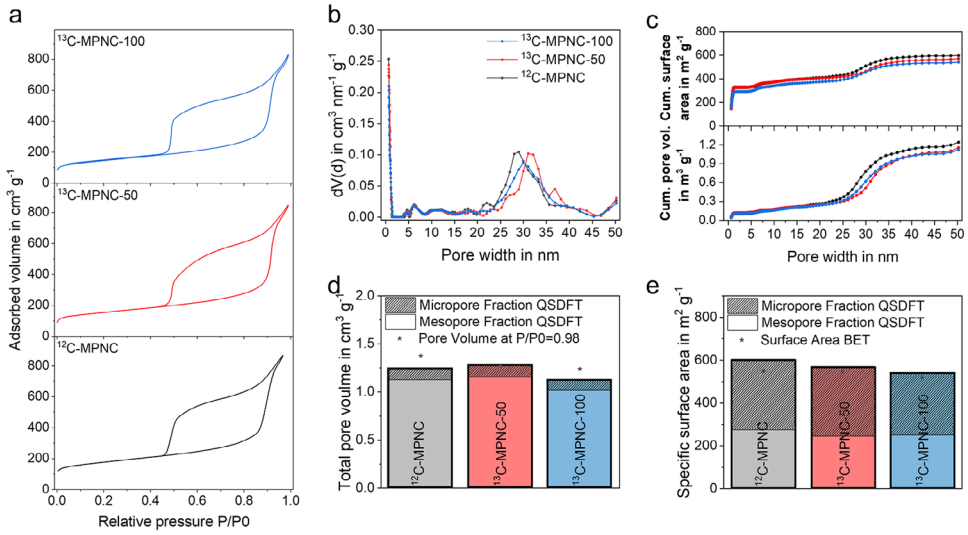

Figure 3. Nitrogen physisorption isotherms (a) (for a bigger version of the isotherms see Figure S2, Supporting Information), pore size distribution (b), cumulative pore volume and surface area (c), the corresponding total pore volume (d) and specific surface area (e) of unlabeled, partially ^{13}C labeled and fully ^{13}C labeled MPNC nanospheres.

all three samples showed a comparable diffractogram, indicating a comparable microstructure.

This result is underlined by the Raman spectra (Figure 2b), which are comparable for all three samples as well. It should be noted that a shift of the spectrum to lower wavenumbers is visible for increased ^{13}C contents due to the higher atomic mass of ^{13}C compared to ^{12}C.[22] The spectra show two main peaks in the wavenumber range of 1540–1605 cm^{-1} and 1305–1365 cm^{-1} that correspond to defect-rich (D1, edges of graphene sheets, point defects, doping, polyaromatic clusters) and defect-free (G) areas of graphene layers. Additionally, three more defect bands need to be fitted (D4 in the range from 1100 to 1160 cm^{-1}, D3 in the range from 1467 to 1533 cm^{-1}, and D2 in the range from 1610 to 1670 cm^{-1}), which are characteristic of disordered carbon materials.[23] An exemplary deconvolution for ^{12}C-MPNC is shown in Figure 2c. The deconvolution for all samples can be found in Figure S1 (Supporting Information).

When comparing the integral areas of the three samples, it becomes evident that the shares of the five bands are comparable in all samples (for all values see Table S1, Supporting Information), indicating that there was no or only minor change of microstructure when the MPNC nanospheres were partially or fully ^{13}C labeled. Especially the integral area of the G band is of high interest here, as its share of the overall integral area of the spectrum is a measure of the degree of graphitization of the sample. In our study, we achieved values of 17.1%, 14.2%, and 16.2% for ^{12}C-MPNC, ^{13}C-MPNC-50, and ^{13}C-MPNC-100, respectively, which are in good agreement with previous results for MPNC nanospheres carbonized at 1000 °C.[5]

The elemental combustion analysis resulted in comparable compositions for all three MPNC nanosphere samples, independent from the degree of labeling (Figure 2e, for all values see Table S2, Supporting Information), leading to carbon, hydrogen, nitrogen, and sulfur contents of 79.0 ± 2.0, 1.4 ± 0.2, 3.5 ± 0.2 and 0.3 ± 0.1 wt.%, respectively.

To determine the surface area as well as pore volume and investigate the pore structure of the three samples, we measured nitrogen physisorption isotherms (**Figure 3**a, for an overlayed representation, please see Figure S2, Supporting Information). All adsorption-desorption isotherms showed a type IV hysteresis, which is typical for mesoporous materials.[24] Based on the measured isotherms we used quenched solid density function theory (QSDFT, adsorption branch only, assuming slit, cylindrical and spherical pores) to calculate the pore size distribution (Figure 3b) as well as cumulative surface area and cumulative pore volume of the samples (Figure 3c). Besides a high content of micropores in all samples, the main mesopore size was determined as 30 ± 1 nm. As the same SiO_2 template was used for all samples, a comparable main mesopore size was expected. Cumulative surface area and pore volume showed similar trends for all three samples, resulting in a total pore volume of 1.09 ± 0.07 cm^3 g^{-1} and a specific surface area of 573 ± 31 m^2 g^{-1}.

The QSDFT model also allowed us to calculate the micropore fraction of the pore volume and surface area. While the fraction was small (0.11 ± 0.01 cm^3 g^{-1}, 10%) for the pore volume, the micropores had a high share (310 ± 20 m^2 g^{-1}, 54%) on the surface area. It should be noted that slight differences in the physisorption results are normal even for repeated measurements of the same sample due to some measurement uncertainties, especially for the mass determination of the samples, which is crucial for the determination of the specific pore volume and surface area. Within the margin of error, we suggest that the measurement results of the nitrogen physisorption measurements are comparable for the three samples. Additionally, the additional weight of the heavier ^{13}C atoms compared to ^{12}C atoms was neglected for the calculation of the specific pore volume and surface area, and thus leads to slightly lower values with increasing ^{13}C content.

In summary, we were successfully able to synthesize three MPNC nanosphere samples, which are unlabeled (^{12}C-MPNC), partially (^{13}C-MPNC-50), and fully (^{13}C-MPNC-100) ^{13}C labeled. All three samples showed comparable particle size distributions,

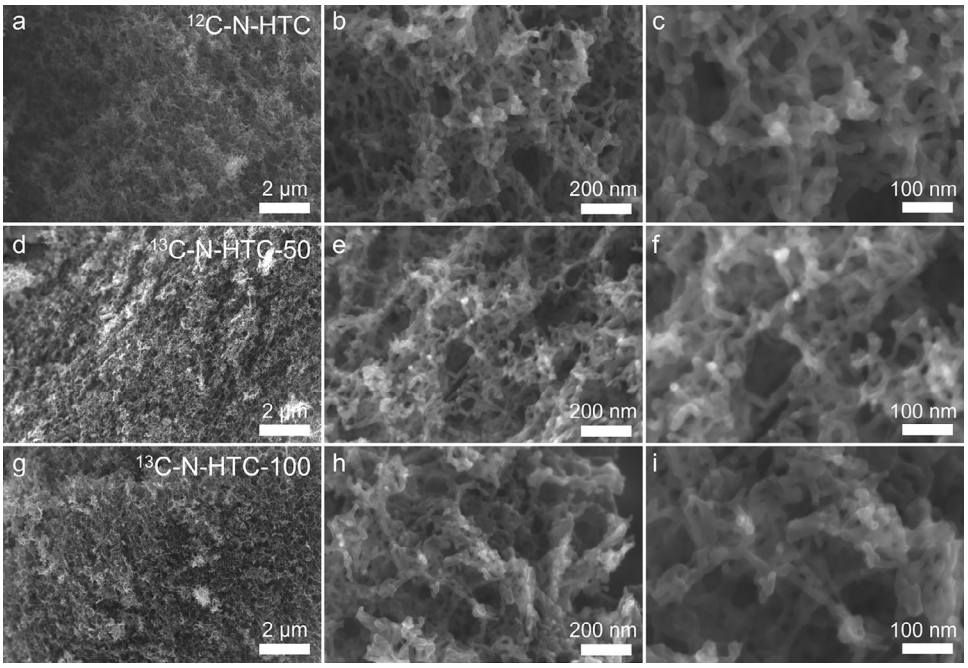

Figure 4. SEM images of unlabeled (a–c), partially ^{13}C-labeled (d–f), and fully ^{13}C-labeled (g–i) N-HTC.

microstructures, and elemental compositions. In nitrogen physisorption experiments, we obtained comparable pore volumes and surface areas for all three samples as well. This clearly shows that ^{13}C labeling of MPNC nanospheres is possible without changing the morphology and physicochemical properties of the nanospheres.

2.2. Unlabeled, Partially ^{13}C Labeled and Fully ^{13}C Labeled N-HTC

Besides the MPNC nanospheres, we used N-doped hydrothermal carbon (N-HTC) as a second model material to investigate ^{13}C labeling. We again synthesized three samples with no (^{12}C-N-HTC), partial (^{13}C-N-HTC-50), and full (^{13}C-N-HTC-100) ^{13}C labeling. SEM measurements (**Figure 4**) revealed coral-like aerogel structures for all three samples. Hereby, the thickness of the coral arms was in the range of (17 ± 2) nm, showing no difference in structure with increasing ^{13}C content.

The microstructure was again investigated by XRD (**Figure 5a**) and Raman spectroscopy (Figure 5b). In addition to the two reflections at $2\theta = 23.5°$ and 43.7° ($\lambda = 1.54$ Å, Cu K_α) that were visible for MPNC nanospheres, N-HTC showed two more visible reflections at 62.0° and 80.3°, which can be assigned to the (004) and (110) reflections. However, no obvious difference was visible

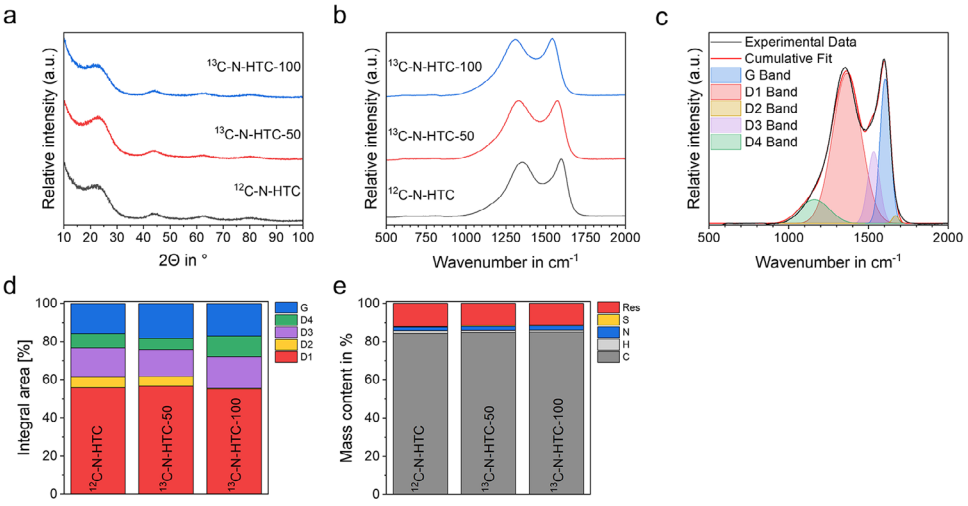

Figure 5. XRD diffractogram (a) and Raman spectrum (b) of unlabeled, partially ^{13}C-labeled, and fully ^{13}C-labeled N-HTC. Exemplary Raman deconvolution (c) for unlabeled N-HTC (for all deconvolutions see Figure S3, Supporting Information) as well as integral areas (d). Elemental composition determined by elemental combustion analysis (e).

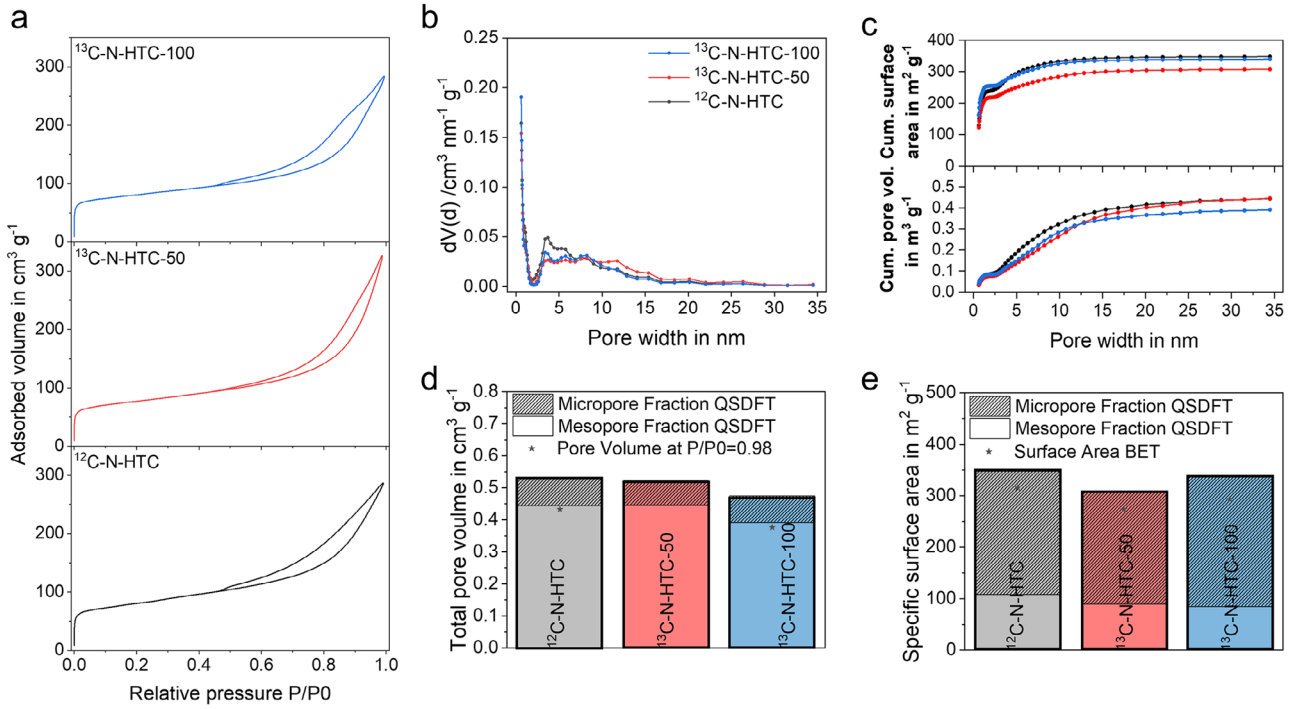

Figure 6. Nitrogen physisorption isotherms (a) (for an overlayed version of the isotherms see Figure S4, Supporting Information), pore size distribution (b), cumulative pore volume and surface area (c), the corresponding total pore volume (d) and specific surface area (e) of unlabeled, partially 13C labeled and fully 13C labeled N-HTC.

between the diffractograms of the three samples. In the Raman spectra, besides the shift in wavenumber (as discussed above), the three samples were comparable as well. The deconvolution of the spectra into five Raman bands (the deconvolution for all samples can be found in Figure S3, Supporting Information) showed only minor differences for the three samples, resulting in a share of the G-band of 17.0 ± 1.2%. The elemental composition as determined by elemental combustion analysis resulted in mass contents of 84.6 ± 0.3, 1.4 ± 0.2, 1.9 ± 0.2, and 0.4 ± 0.1 wt.% for carbon, hydrogen, nitrogen, and sulfur, respectively.

Finally, we investigated the porosity of the samples by nitrogen physisorption (**Figure 6**). Compared to MPNC nanospheres, N-HTC still shows type IV adsorption-desorption isotherms, but with a much smaller hysteresis between adsorption and desorption isotherms, indicating less porosity in the mesopore range (Figure 6a, for a bigger depiction, please see Figure S4, Supporting Information). The shape of the isotherm hereby gives information about the pore type, with the present hysteresis being typical for slit pores. Additionally, the nearly linear middle section of the isotherms indicates macropores, where multilayer condensation on the sample surface occurs.[24] These correlate well with the results from the SEM images, where mainly small mesopores between multiple coral arms and macropores between the coral structures were visible. The QSDFT calculations showed a high amount of micropores below 2 nm and only a minor contribution of mesopores in the pore size distribution (Figure 6b). For all three samples, the pore size distributions showed similar trends with only slight differences in the mesopore range, leading to slightly higher pore volumes and surface areas for the unlabeled sample.

Compared to MPNC nanospheres, N-HTC had a lower total pore volume and specific surface area, showing values of only 0.43 ± 0.03 cm^3 g^{-1} and 297 ± 17 m^2 g^{-1}, while most of the surface area results from micropores (Figure 6c–e). It is noteworthy that the N-HTC synthesis is based on natural materials like glucose and ovalbumin, being processed under hydrothermal conditions, and thus these slight differences in the porosity occur naturally during the synthesis process and can't be attributed to the labeling process itself.

In summary, we were able to synthesize N-HTC with no (^{12}C-N-HTC), partial (^{13}C-N-HTC-50), and full (^{13}C-N-HTC-100) ^{13}C labeling that showed similar morphology and physicochemical properties, with only minor variations in composition and porosity.

2.3. Evaluation of Carbon Electrode Degradation by Electrochemical Mass Spectrometry

To study carbon corrosion and the effect of ^{13}C labeling on our materials under accelerated stress test conditions (carbon AST), we prepared MPNC nanospheres and N-HTC containing inks, which were subsequently coated and dried on glassy carbon electrodes. These electrodes were then inserted into the three-electrode electrochemical setup of an EC-MS system, which was connected to a mass spectrometer by a specialized gas-permeable silicon chip. This allowed us to determine the evolution of gaseous species (and especially CO_2) time resolved and couple this data with our electrochemical experiments.

Accelerated carbon stress tests were performed by applying a defined constant potential (in the range of 1.0 to 1.6 V vs. RHE for MPNC nanospheres and in the range of 1.0 to 1.7 V vs. RHE for N-HTC, with a resolution of 100 mV) for 2 min before switching to a relaxation potential of 0.05 V vs RHE for 6 min to allow all formed gaseous species to diffuse through the silicon chip into the mass spectrometer.

The qualitative EC-MS results for unlabeled (^{12}C-MPNC), partially (^{13}C-MPNC-50), and fully (^{13}C-MPNC-100) ^{13}C-labeled MPNC nanospheres, as well as a physical 50:50 mixture of unlabeled and fully labeled MPNC nanospheres (^{12}C-MPNC + ^{13}C-MPNC-100) can be seen in **Figure 7**. It should be noted that our study did not aim to fully quantify the CO_2 evolved from carbon corrosion, but rather to demonstrate the effect of ^{13}C labeling in the materials in distinguishing between $^{12}CO_2$ and $^{13}CO_2$.

The first column of the Figure exemplarily shows the applied potential and resulting current for the different MPNC nanospheres at an applied potential of 1.6 V vs RHE. The current response followed the applied voltage for all materials and showed a current spike as soon as the potential was increased. Over time, this current then exponentially decreased until it plateaued. As soon as the potential decreased to 0.05 V vs RHE again, the current response spiked to negative values before quickly relaxing to no current flow. While the current spikes at the start and end of the applied potential period can be attributed to the charge of the electrochemical double layer, the plateau at the end of the applied potential period correlates with the carbon corrosion rate and is comparable around 10–15 µA for all four samples.

By coupling the signals of the mass spectrometer for $^{12}CO_2$ (M44) and $^{13}CO_2$ (M45) (Figure 7b,e,h,k), it becomes evident that CO_2 evolution was only detectable under applied potential. In case of unlabeled MPNC nanospheres (Figure 7b), only $^{12}CO_2$ and no $^{13}CO_2$ were detected, while for fully labeled MPNC nanospheres (Figure 7e), only $^{13}CO_2$ and no $^{12}CO_2$ were detected. It should be mentioned that the unlabeled sample still contained the natural amount of 1.1% ^{13}C, but this amount was too low to detect it with the EC-MS setup. In case of the partially labeled MPNC nanospheres and the 50:50 mixture of unlabeled and fully labeled MPNC nanospheres, both CO_2 species could be detected simultaneously. An overview of the time-dependent mass spectrometer signal for all applied potentials can be taken from Figure S5 (Supporting Information). It is noteworthy that the second potential cycle for a given potential often resulted in slightly higher signal intensities of the mass spectrometer. We attribute this effect to a pre-oxidation of the carbon materials in the first cycle, which can then be fully oxidized to CO_2 in the second cycle much more easily. Additionally, formed CO_2 could be trapped in the porosity of the carbon electrode and only released after more CO_2 is formed in the second potential cycle.

Finally, the potential dependent maximal normalized intensity of the mass spectrometer signal can be taken from the last column of Figure 7. It should be noted that the mass spectrometer signals from different experiments are not quantitatively comparable. The signal intensities were normalized to simplify the comparison between samples, as the signal intensity of the mass spectrometer is very sensitive, and even exchange of the carbon-coated working electrode or the quality of the coated carbon film on the electrode could lead to changed signal intensities. Again, the trend as a function of the applied potential was comparable for all samples, showing starting CO_2 evolution at 1.3 V vs RHE for all samples, which was increased exponentially with increasing applied potential.

As for the time-dependent CO_2 evolution, in the case of unlabeled MPNC nanospheres, only $^{12}CO_2$ was detected, while only $^{13}CO_2$ was detected for the fully labeled MPNC nanospheres. For the partially labeled sample, comparable signal intensities of $^{12}CO_2$ and $^{13}CO_2$ were found. The same is true for the physical mixture of unlabeled and fully labeled MPNC nanospheres.

It is noteworthy that slight differences in the intensities of $^{12}CO_2$ and $^{13}CO_2$ were found for the chemical and physical mixtures. The slightly lower $^{13}CO_2$ intensities compared to the $^{12}CO_2$ intensities might be explained by kinetic isotope effects (*KIE*). Formally, the *KIE* is the ratio of the reactions involving the light (here: k_{12C}) and the heavy (k_{13C}) isotopically substituted reactants:

$$KIE = \frac{k_{12}}{k_{13}} \tag{3}$$

In general, isotopes with higher atomic mass have a lower vibrational energy and thus have slower reaction kinetics compared to isotopes with lower atomic mass.[25–27] Depending on the overall mass of the isotopes, this effect can be more or less distinct. In case of ^{12}C and ^{13}C, the mass of ^{13}C is 1.083 times higher than the mass of ^{12}C, and hence could lead to slightly lower corrosion rates. To the best of our knowledge, there are no reported kinetic isotope effects of ^{13}C specifically for carbon corrosion, but other chemical reactions and enzymatic processes involving ^{13}C kinetic isotope effects have been reported. However, typical *KIE* values reported for heavy atoms (here ^{13}C) are in the range of 1.00–1.05 and clearly indicate only a very small change in reaction rate.

To fully unravel, isotope effects in our study, the qualitatively described results would need to be quantified. However, calibration of the EC-MS with calibration gas mixtures is far from trivial, as $^{13}CO_2$ gas mixtures with $^{13}CO_2$ concentrations as low as those resulting from carbon corrosion are (to the best of our knowledge) not easily available on the market. In conclusion, isotope effects on the corrosion rate of ^{13}C-labeled samples in our study are possible, but our results do not conclude that ^{13}C-labeled MPNC nanospheres have a different carbon corrosion rate than unlabeled MPNC nanospheres.

The EC-MS experiments were repeated for the second developed carbon material using unlabeled (^{12}C-N-HTC), partially (^{13}C-N-HTC-50), and fully (^{13}C-N-HTC-100) ^{13}C-labeled N-HTC, as well as a physical 50:50 mixture of unlabeled and fully ^{13}C-labeled N-HTC (**Figure 8**). As for MPNC nanospheres, a current was only measured when high potentials were applied, and the detection of $^{12}CO_2$ in the case of unlabeled N-HTC and $^{13}CO_2$ in the case of fully labeled N-HTC was only possible while potentials were applied. In contrast to MPNC nanospheres, where CO_2 evolution already started at a potential of 1.3 V vs RHE, N-HTC showed a starting carbon corrosion at 1.4 V vs RHE, demonstrating a slightly higher carbon corrosion stability compared to MPNC nanospheres.

Again, the signal intensity of the mass spectrometer increased when the applied potential was increased. For partially ^{13}C-labeled N-HTC and the physical 50:50 of unlabeled and

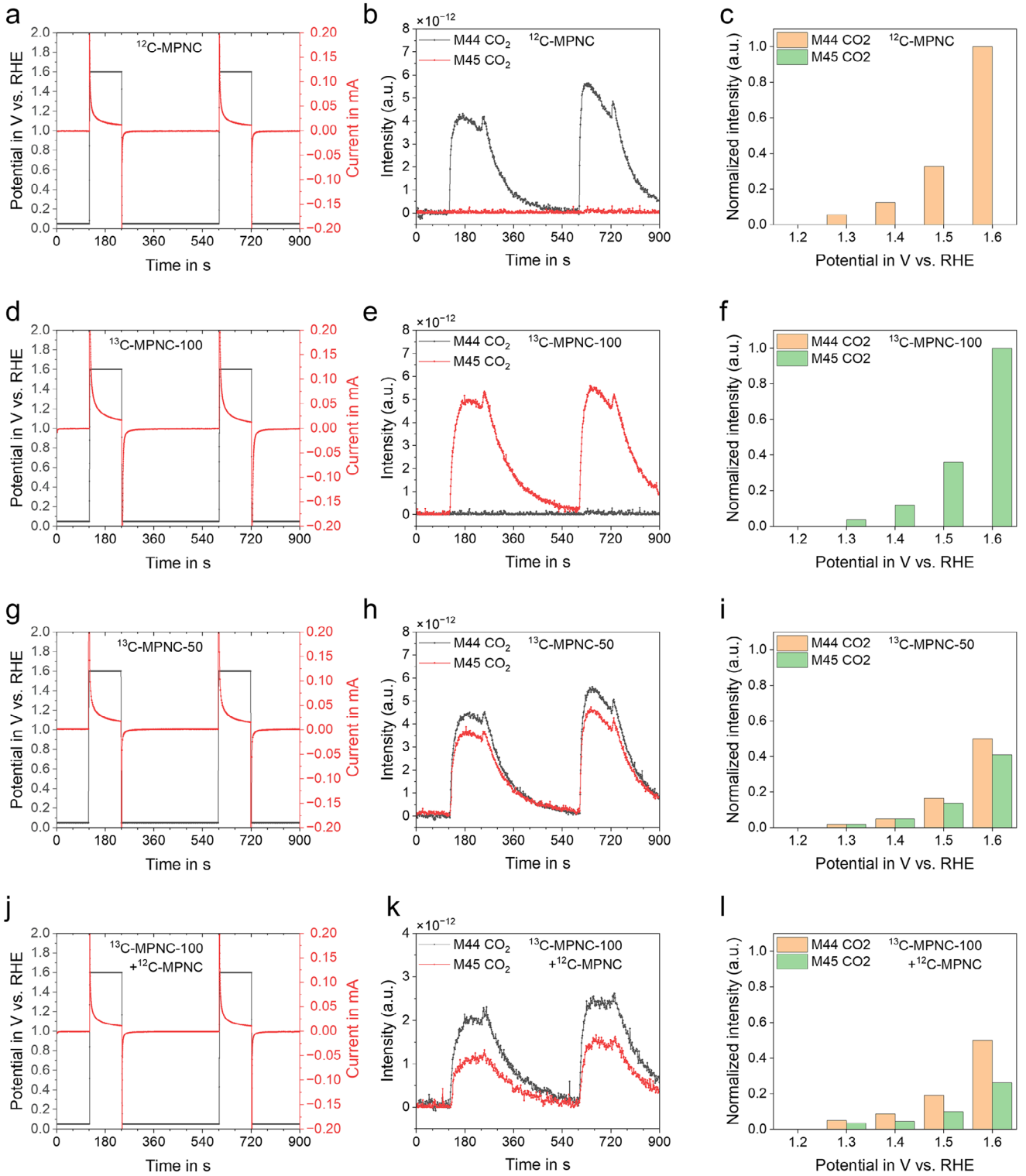

Figure 7. Electrochemical mass spectrometry measurements for unlabeled (a–c) and fully ^{13}C labeled MPNC nanospheres (d–f), 50% ^{13}C labeled MPNC nanospheres (g–i) and a physical 50:50 mixture of unlabeled and fully ^{13}C labeled MPNC nanospheres (j–l), with the applied potential and resulting current, time dependent $^{12}CO_2$ (M44) and $^{13}CO_2$ (M45) evolution at an applied potential of 1.6 V vs RHE, and potential dependent maximal $^{12}CO_2$ and $^{13}CO_2$ evolution.

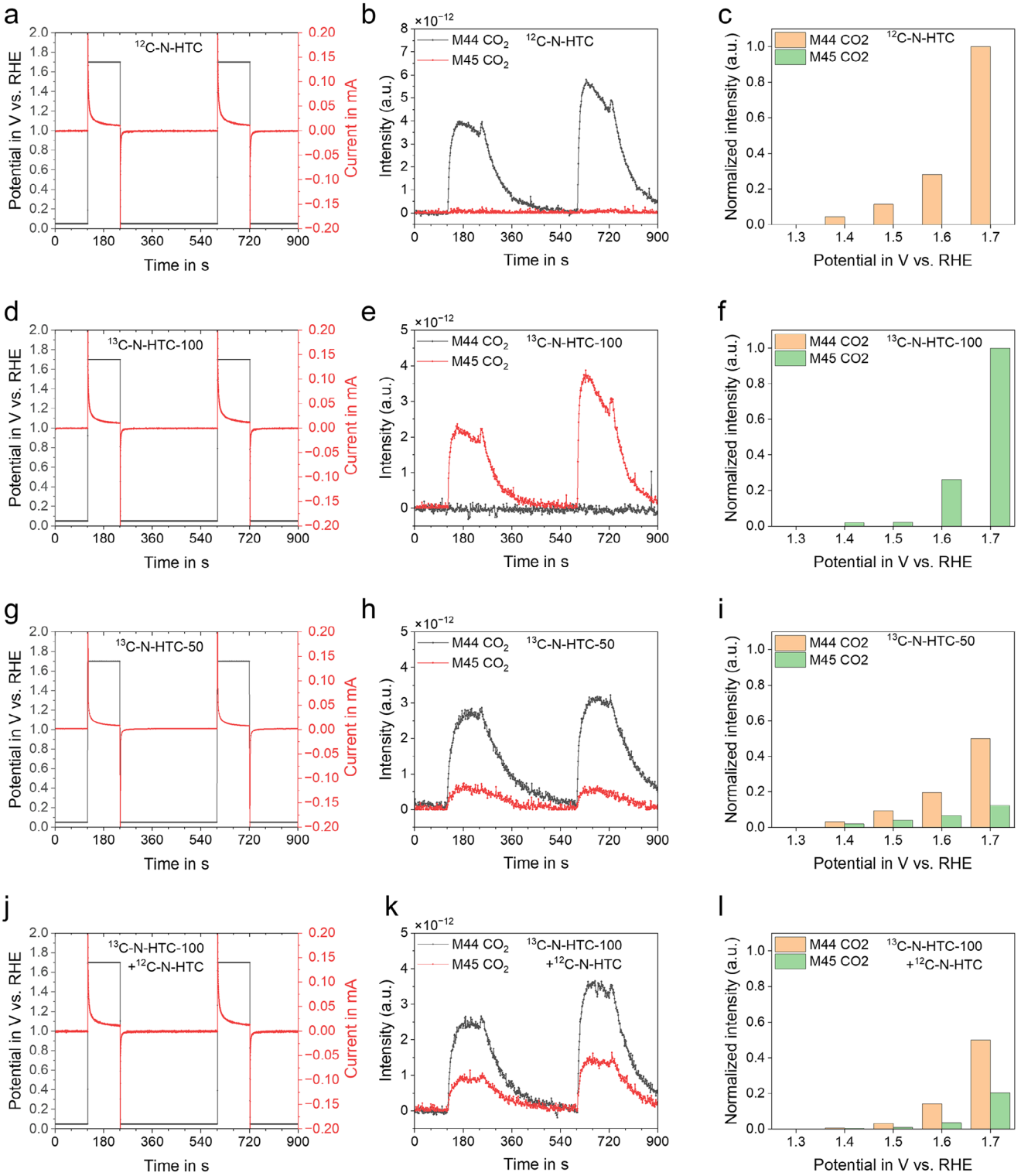

Figure 8. Electrochemical mass spectrometry measurements for unlabeled (a–c) and fully ^{13}C labeled N-HTC (d–f), 50% ^{13}C labeled N-HTC (g–i) and a physical 50:50 mixture of unlabeled and fully ^{13}C labeled N-HTC (j–l), with the applied potential and resulting current, time-dependent $^{12}CO_2$ (M44) and $^{13}CO_2$ (M45) evolution, and potential-dependent maximal $^{12}CO_2$ and $^{13}CO_2$ evolution.

fully ^{13}C-labeled N-HTC, again, $^{12}CO_2$ and $^{13}CO_2$ were detected side by side. An overview of the time-dependent mass spectrometer signal for all applied potentials can be taken from Figure S6 (Supporting Information).

In summary, we were able to show in our EC-MS studies that carbon corrosion in our electrodes only occurred at elevated potentials above 1.3 V vs RHE and increased exponentially with increasing potential. While carbon corrosion was already visible at this potential for MPNC nanospheres, a potential of 1.4 V vs RHE was required in the case of N-HTC. Independently of the used carbon material, an increased amount of ^{13}C labeling led to increased detected intensities of $^{13}CO_2$. Additionally, there was no visible difference between partially labeled carbon materials and physical 50:50 mixtures of unlabeled and fully ^{13}C-labeled materials. We therefore suggest that the amount of labeling does not significantly affect the carbon corrosion of the synthesized materials and that it does not make a major difference whether the amount of labeling is controlled via the ^{12}C to ^{13}C ratio in the synthesis or the physical mixture of unlabeled and fully labeled MPNC nanospheres. A full quantification of the expected small kinetic isotopic effect requires different experimental characterisation. This work is planned when these carbons are applied as catalyst supports in PEMFC.

3. Conclusion

In this study, we used mesoporous N-doped carbon (MPNC) nanospheres and hydrothermal N-doped carbon (N-HTC) as model materials to investigate the effect of ^{13}C labeling on the physicochemical properties of carbon support materials. We then used these materials with different amounts of ^{13}C labeling as well as physical mixtures of unlabeled and fully labeled materials in EC-MS studies using accelerated carbon stress tests (carbon AST) to investigate the effect of ^{13}C labeling on the detection of $^{12}CO_2$ and $^{13}CO_2$ as the main products of carbon corrosion.

For MPNC nanospheres, all analyzed physicochemical parameters were constant independently of the amount of ^{13}C labeling, showing that diagnostic ^{13}C labeling can be introduced into the carbon structure without changing the material properties. In case of N-HTC, the physicochemical parameters of the samples with different amounts of ^{13}C labeling were similar to each other, but showed slight differences due to the solvothermal synthesis and fluctuations of the used natural raw products. This, however, could not be contributed to the amount of ^{13}C labeling. For both carbons, no systematic kinetic isotope effect on the physicochemical properties of the materials was found.

In the carbon corrosion EC-MS studies, formation of CO_2 was only obtained for applied potentials starting at 1.3 V vs RHE in the case of MPNC nanospheres and 1.4 V vs RHE for more stable N-HTC. Independently of the used material or amount of ^{13}C labeling, the rate of CO_2 formation increased with increasing applied potential. While for the unlabeled samples only $^{12}CO_2$ was detected, only $^{13}CO_2$ was detected for the fully ^{13}C-labeled samples. In case of partially ^{13}C-labeled samples or 50:50 mixtures of unlabeled and fully ^{13}C-labeled samples $^{12}CO_2$ and $^{13}CO_2$ could be detected simultaneously. We therefore conclude that it does not make a major difference whether the amount of labeling is controlled via the ^{12}C to ^{13}C ratio in the synthesis or the physical mixture of unlabeled and fully ^{13}C-labeled carbon materials.

In summary, our study demonstrated that ^{13}C labeling of MPNC nanospheres and N-HTC is possible without changing the morphology and physicochemical properties of the materials. These ^{13}C-slabeled materials can now be used as diagnostic carbon twins in different applications, such as in PEMFC to study the stability of catalyst carbon supports by in situ $^{13}CO_2$ carbon corrosion measurements, or to study electrode materials or additive degradation in aqueous supercapacitors or batteries.

4. Experimental Section

Synthesis of Mesoporous N-Doped Carbon Nanospheres: MPNC nanospheres were synthesized as reported previously.[5] 400 mL MilliQ H_2O was transferred into a 1000 mL round-bottom flask and cooled down in an ice bath. 50 mL 1M•HCl, 4 mL aniline, and 11.5 mL colloidal silica were added subsequently, and the mixture was stirred until a homogeneous solution was formed. In the meantime, 10.02 g ammonium persulfate (APS) was dissolved in 20 mL 1 M•HCl. To induce polymerization of aniline, the APS solution was added to the round-bottom flask dropwise over 15 min by using a dropping funnel. The mixture was then stirred for 24 h while keeping the reaction flask cooled in the ice bath.

The formed PANI/SiO_2 composite polymer particles were collected by centrifugation (9000 rpm, 10 min) and redispersed in fresh water. This washing step was repeated at least 10 times until the pH of the solution was neutral, and the obtained nanocomposite material was subjected to freeze-drying to prevent morphology change. The freeze-dried powder was then transferred to a calcination boat and heated to 1000 °C under a nitrogen atmosphere with a heating ramp of 200 K h^{-1} and a holding time of 6 h. To remove the silica template from the carbonized sample, the composite material was etched with 4M•NH_4HF_2 solution (50 mL g^{-1} of sample) for 48 h, resulting in MPNC nanospheres. The MPNC was separated from the etching solution by filtration, and the filter cake was redispersed in fresh H_2O and stirred for 12 h to wash out any NH_4HF_2 residuals. This washing step was repeated four times, followed by washing with ethanol. The washed MPNC was dried under vacuum for 24 h, and the resulting dry powder was annealed at 500 °C under a nitrogen atmosphere with a heating ramp of 200 K•h^{-1} for 2 h. The final MPNC powder was recovered with a yield of 1.76 g (43%) and was denoted as ^{12}C-MPNC.

Partially and fully 13C-labeled MPNC were synthesized by replacing either 50% or 100% of the used aniline with fully ^{13}C-labeled aniline. The resulting samples were denoted as ^{13}C-MPNC-50 and ^{13}C-MPNC-100 and were recovered with yields of 1.64 g (40%) and 1.60 g (39%), respectively.

Synthesis of N-Doped Hydrothermal Carbon: MPNC nanospheres were synthesized as reported previously.[17] 1.5 g glucose and 0.3 g ovalbumin were transferred into a 45 mL glass tube. 13.5 mL MilliQ H_2O was added, and the mixture was stirred until a homogeneous solution was formed, before the glass tube was placed in a Teflon-inlet lined 45 mL steel autoclave and heated to 180 °C for 5.5 h in a heating furnace.

The formed carbon monolith was washed in excess with fresh water and ethanol. This washing step was repeated at least 10 times until the pH of the solution was neutral. The obtained carbon material was subjected to freeze-drying to prevent morphology change. 300 mg of the freeze-dried carbon material was transferred to a calcination boat and heated to 1000 °C under a nitrogen atmosphere with a heating ramp of 200 K h^{-1} and a holding time of 6 h. After the carbonization step, the product was ground down with a mortar. The final N-HTC powder was recovered with a yield of 40% and was denoted as ^{12}C-N-HTC.

Partially and fully ^{13}C-labeled N-HTC were synthesized by replacing either 50% or 100% of the used glucose with fully ^{13}C-labeled glucose. The resulting samples were denoted as ^{13}C-N-HTC-50 and ^{13}C-N-HTC-100 and were recovered with yields of 42% and 39%, respectively.

Material Characterization: Scanning Electron Microscopy (SEM) images were obtained using a Field Emission Gun High Resolution SEM (FEG-HRSEM) SU8220 (Hitachi) equipped with an SE (secondary electron) and TE (transmission electron) detector. For sample preparation, a

small amount of the powder sample was dispersed in isopropanol, and the diluted suspensions were drop-cast onto carbon-coated copper grids (200 mesh). Alternatively, a larger amount of the powder sample was directly placed on top of a double-sided conductive tape attached to the sample holder. For general imaging, the scanning mode was used with an acceleration voltage of 2.5 kV and a working distance of 3.0 mm was applied. To investigate the porosity of MPNC samples, the transmission mode was used, operated at an acceleration voltage of 30 kV and a working distance of 8.0 mm. Particle sizes of at least 200 MPNC particles or coral diameters of at least 200 N-HTC coral arms were counted with the image J software.

The polydispersity index (PDI) of the MPNC nanospheres was calculated according to the IUPAC definition using Equation (4), where N_i denotes the number of particles with the diameter d_i:[20]

$$PDI = \frac{\sum N_i \sum N_i d_i^4}{\sum N_i d_i \sum N_i d_i^3} \quad (4)$$

X-ray diffraction was measured on a Bruker D8 Discover using a flat sample holder. The sample was measured under rotation with 15 rpm, and the diffractogram was recorded between 10° and 105° 2Θ with a step size of 0.025° and a measurement time of 0.5 s per step. For each sample, three individual measurements were obtained and averaged.

Raman spectra were recorded using a Senterra II microscope (Bruker) equipped with a 532 nm laser. The laser power was set to 0.25 mW, and measurements were performed in the range of 750–2500 cm^{-1} with a wavenumber resolution of 4 cm^{-1}. Fitting of the spectra between 1000 and 1800 cm^{-1} was done with the Origin Lab 2024 software. For each sample, three individual measurements were obtained and averaged.

Elemental combustion analysis was carried out on a Vario MICRO cube (Elementar Analysensysteme GmbH) system equipped with a temperature programmable column and a thermal conductivity detector. Roughly 1 mg of sample was mixed with the same amount of WO_3 as an oxidation catalyst and combusted at 1150 °C.

The specific surface area and pore structure were determined by N_2 physisorption at 77 K using an Autosorb 1-C physisorption station (Quantachrome). Before the measurement, powder samples were degassed in a vacuum at 100 °C for 24 h. Specific surface areas were calculated using the Brunauer–Emmer–Teller (BET) method, fitting the P/P_0 range from 0.05 to 0.30. Pore size distributions were determined according to quenched solid density functional theory (QSDFT), considering slit, cylindrical and spherical pores. The micropore specific surface areas and pore volumes were estimated using the t-plot method and QSDFT equilibrium model.

Preparation of Electrodes: To prepare carbon film electrodes, ≈3 mg carbon powder was mixed with 995 µL water and 250 µL isopropanol as a solvent and 5 µL Nafion solution (5 wt.%) as a binder. The mixture was then tip sonicated for at least 30 min (40% amplitude, 2 s on-time, 2 s off-time). 10 µL of the resulting ink was drop-coated on a rotation disk electrode (RDE, 5 mm diameter) and dried under rotation. After the film had dried, the RDE was transferred to a drying oven and was kept there for 30 min at 60 °C.

Four different MPNC inks and therefore four types of electrodes were prepared: ^{12}C-MPNC (unlabeled), ^{13}C-MPNC-100 (fully labeled), ^{13}C-MPNC-50 (partially labeled) and a 50:50 mixture of ^{12}C-MPNC and ^{13}C-MPNC-100. Additionally, the same inks were prepared with N-HTC: ^{12}C-N-HTC, ^{13}C-N-HTC-100, ^{13}C-MPNC-50 and a 50:50 mixture of ^{12}C-N-HTC and ^{13}C-N-HTC-100.

Electrochemical Mass Spectrometry Measurements: The prepared electrodes were inserted into an EC-MS measurement system from Spectroinlets as a working electrode. A platinum mesh was used as a counter electrode, a reversible hydrogen electrode (RHE) was used as a reference electrode and 0.5 M perchloric acid was used as the electrolyte. The electrolyte was degassed in situ with helium (1 mL min^{-1}), which was used as carrier gas in the EC-MS system.

To perform the carbon stress test, a defined constant potential was applied over 2 min, and the current response as well as the MS signals of $^{12}CO_2$ (M44) and $^{13}CO_2$ (M45) were detected over this time period. After relaxation of the MS signal, the constant potential was applied a second time for another 2 min, followed by another relaxation period. This process was repeated for increasing potentials of 1.0, 1.1, 1.2, 1.3, 1.4, 1.5, 1.6 and 1.7 V vs RHE, while the potential in the relaxation period was set to 0.05 V vs RHE.

Supporting Information

Supporting Information is available from the Wiley Online Library or from the author.

Acknowledgements

This research was funded as part of the "H2MARINE" and "CLEANER" projects and by core funding of the University of Freiburg.

The "H2MARINE" project is supported by the Clean Hydrogen Partnership and its members Hydrogen Europe and Hydrogen Europe Research under grant agreement No 101137965 funded by the European Union and the Swiss State Secretariat for Education Research and Innovation. Views and opinions expressed are however those of the authors only and do not necessarily reflect those of the European Union or Clean Hydrogen Joint Undertaking. Neither the European Union nor Clean Hydrogen Joint Undertaking can be held responsible for them.

The "CLEANER" project is supported by the Clean Hydrogen Partnership and its members under the grant agreement No 101137799. The project is co-funded by the Research Council of Norway and the UK Research and Innovation (UKRI) under the UK government's Horizon Europe funding guarantee. Views and opinions expressed are however those of the author(s) only and do not necessarily reflect those of the European Union or Clean Hydrogen JU. Neither the European Union nor the granting authority can be held responsible for them.

Open access funding enabled and organized by Projekt DEAL.

Conflict of Interest

The authors declare no conflict of interest.

Author Contributions

N.O. and J.M. contributed equally to this work. A.F. and J.I. initiated this research. A.F. designed the present research, acquired funding and provided the required resources. A.F., N.O. and J.M. designed the experiments. N.O. synthesized the (meso)porous *N*-doped carbon nanospheres and performed material characterization. J.M. synthesized the hydrothermal carbons and performed material characterization. L.G. prepared electrodes and performed EC-MS experiments. A.F. supervised the project. A.F., N.O. and J.M. designed the storyline of the manuscript, while N.O. and J.M. wrote the manuscript with the input from all authors. All authors discussed the results and revised the manuscript and have given approval to its final version.

Data Availability Statement

The data that support the findings of this study are available from the corresponding author upon reasonable request.

Keywords

^{13}C-labeling, carbon corrosion, EC-MS, mesoporous N-doped carbon nanospheres, N-doped hydrothermal carbon aerogels

Received: December 30, 2024
Revised: April 13, 2025
Published online:

[1] A. Narimisa, *Adv. Mater. Sci. Res.* **2024**, *7*, 189.
[2] R. Sanjinés, M. D. Abad, C. Vâju, R. Smajda, M. Mionić, A. Magrez, *Surf. Coat. Technol.* **2011**, *206*, 727.
[3] D. Sheng Su, G. Centi, *J. Energy Chem.* **2013**, *22*, 151.
[4] Z. Heidarinejad, M. H. Dehghani, M. Heidari, G. Javedan, I. Ali, M. Sillanpää, *Environ. Chem. Lett.* **2020**, *18*, 393.
[5] N. Ortlieb, T. Berestok, P. Elsässer, R. Thomann, M. Knäbbeler-Buß, A. Fischer, *Small* **2024**, *21*, 2407235.
[6] A. Rützler, J. Büttner, J. Oechsler, S. E. Balaghi, S. Küspert, N. Ortlieb, A. Fischer, *Adv. Funct. Mater.* **2024**, *34*, 2401188.
[7] Z. Zeng, S. Küspert, S. E. Balaghi, H. E. M. Hussein, N. Ortlieb, M. Knäbbeler-Buß, P. Hügenell, S. Pollitt, N. Hug, J. Melke, A. Fischer, *Small* **2023**, *19*, 2205885.
[8] S. A. Nicolae, H. Au, P. Modugno, H. Luo, A. E. Szego, M. Qiao, L. Li, W. Yin, H. J. Heeres, N. Berge, M. M. Titirici, *Green Chem.* **2020**, *22*, 4747.
[9] S. Maass, F. Finsterwalder, G. Frank, R. Hartmann, C. Merten, *J. Power Sources* **2008**, *176*, 444.
[10] X. Yu, S. Ye, *J. Power Sources* **2007**, *172*, 145.
[11] N. Macauley, D. D. Papadias, J. Fairweather, D. Spernjak, D. Langlois, R. Ahluwalia, K. L. More, R. Mukundan, R. L. Borup, *J. Electrochem. Soc.* **2018**, *165*, F3148.
[12] H. Chen, X. Zhao, T. Zhang, P. Pei, *Energy Convers. Manag.* **2019**, *182*, 282.
[13] C. Cremers, T. Jurzinsky, J. Meier, A. Schade, M. Branghofer, K. Pinkwart, J. Tübke, *J. Electrochem. Soc.* **2018**, *165*, F3307.
[14] D. R. Lide, in *CRC Handbook of Chemistry and Physics*, 95th ed., CRC Press, Boca Raton, FL, USA, **2014**.
[15] M. Metzger, C. Marino, J. Sicklinger, D. Haering, H. A. Gasteiger, *J. Electrochem. Soc.* **2015**, *162*, A1123.
[16] M. Metzger, J. Sicklinger, D. Haering, C. Kavakli, C. Stinner, C. Marino, H. A. Gasteiger, *J. Electrochem. Soc.* **2015**, *162*, A1227.
[17] J. Martin, J. Melke, C. Njel, A. Schökel, J. Büttner, A. Fischer, *ChemElectroChem* **2021**, *8*, 4835.
[18] J. Melke, R. Schuster, S. Möbus, T. Jurzinsky, P. Elsässer, A. Heilemann, A. Fischer, *Carbon N Y* **2019**, *146*, 44.
[19] S. Küspert, I. E. Campbell, Z. Zeng, S. E. Balaghi, N. Ortlieb, R. Thomann, M. Knäbbeler-Buß, C. S. Allen, S. E. Mohney, A. Fischer, *Small* **2024**, *20*, 2311260.
[20] S. Slomkowski, J. V. Alemán, R. G. Gilbert, M. Hess, K. Horie, R. G. Jones, P. Kubisa, I. Meisel, W. Mormann, S. Penczek, R. F. T. Stepto, *Pure Appl. Chem.* **2011**, *83*, 2229.
[21] Z. Q. Li, C. J. Lu, Z. P. Xia, Y. Zhou, Z. Luo, *Carbon N Y* **2007**, *45*, 1686.
[22] S. D. Costa, C. Fantini, A. Righi, A. Bachmatiuk, M. H. Rümmeli, R. Saito, M. A. Pimenta, *Carbon N Y* **2011**, *49*, 4719.
[23] A. Sadezky, H. Muckenhuber, H. Grothe, R. Niessner, U. Pöschl, *Carbon N Y* **2005**, *43*, 1731.
[24] K. S. W. Sing, D. H. Everett, R. A. W. Haul, L. Moscou, R. A. Pierotti, J. Rouquerol, T. Siemieniewska, *Pure Appl. Chem.* **1985**, *57*, 603.
[25] À. González-Lafont, J. M. Lluch, *Wiley Interdiscip. Rev.: Comput. Mol. Sci.* **2016**, *6*, 584.
[26] K. Karandashev, Z. H. Xu, M. Meuwly, J. Vaníček, J. O. Richardson, *Struct. Dyn.* **2017**, *4*, 061501.
[27] S. E. Scheppele, *Chem. Rev.* **1972**, *72*, 511.